Euler Calculations for Multielement Airfoils Using Cartesian Grids

D. Keith Clarke*
North Carolina State University, Raleigh, North Carolina
M.D. Salas†
NASA Langley Research Center, Hampton, Virginia
and
H.A. Hassan‡
North Carolina State University, Raleigh, North Carolina

A finite volume formulation for the Euler equations using Cartesian grids is presented and used to study complex two-dimensional configurations. The formulation extends methods developed for the potential equation to the Euler equations. Results using this approach for single-element airfoils are shown to be competitive with, and as accurate as, other methods that employ mapped grids. Further, it is demonstrated that this method provides a simple and accurate procedure for solving flow problems involving multielement airfoils.

Introduction

THE need to satisfy the boundary conditions exactly led to the development of body-fitted coordinates.[1] Such coordinates are difficult to generate for complex bodies. Even when they are generated, one has to contend with singularities that require special treatment. Further, when patching techniques are employed, one has to develop adequate interpolation schemes at the various grid boundaries. The introduction of finite volume techniques made it possible to satisfy the wall boundary conditions exactly (in an integral sense), irrespective of the shape of the boundary.[2,3] However, the success of such methods requires elements with smoothly varying sizes and a minimum of skewness. In an effort to avoid the above problems, Purvis and Burkhalter,[4] and later Wedan and South,[5] solved the two-dimensional potential equation using a finite volume formulation and Cartesian grids. The simplicity and utility of the method was demonstrated in Ref. 5 by calculating external flows past lifting and nonlifting bodies for a wide range of Mach numbers and for two-dimensional and axisymmetric internal flows.

The objectives of this work are threefold. The first is to show that the methods of Refs. 4 and 5 for the solution of the potential equation can be extended to the Euler equations using simple procedures. The second is to show that the solution of the Euler equations using this approach is competitive with, and as accurate as, other methods that employ body-fitted grids. Finally, it is demonstrated that the method is capable of solving problems involving multielement airfoils.

There is a major difference in the implementation of boundary conditions between the Euler equations formulation and that of the potential. This is a result of the appearance in the Euler formulation of a wall pressure term that has to be specified in terms of the other flux terms before one can start the calculations. Because of this, the solution process cannot be marched through the body as was done in Ref. 5.

The method developed here can be employed with any number of existing algorithms for the calculations of the Euler equations. It is generally acknowledged that the algorithm developed by Jameson et al.,[6] which employs a Runge-Kutta time stepping scheme is, at present, one of the most efficient algorithms. The procedure employed here makes use of a similar algorithm. The code developed does not employ multigrid or any of the recent improvements developed by Jameson and Baker.[7,8] Thus, the comparisons made here for single-element airfoils employ the version of FL052 described by Salas et al.[9]

Analysis

Governing Equations

The Euler equations in two dimensions can be written as

$$\frac{\partial w}{\partial t}+\frac{\partial f}{\partial x}+\frac{\partial g}{\partial y}=0 \tag{1}$$

where x and y are the Cartesian coordinates and

$$w=[\rho, \rho u, \rho v, \rho E]^t \tag{2}$$

$$f=[\rho u, \rho u^2+p, \rho uv, \rho uH]^t \tag{3}$$

$$g=[\rho v, \rho uv, \rho v^2+p, \rho vH]^t \tag{4}$$

The quantities ρ, p, u, v are the density, pressure, and velocity components in the x and y directions, while E and H are the total energy and total enthalpy per unit mass. For a perfect gas,

$$E=[p/(\gamma-1)\rho]+\tfrac{1}{2}(u^2+v^2)$$

$$H=E+p/\rho$$

$$p=R\rho T \tag{5}$$

where T is the temperature, R the gas constant, and γ the ratio of specific heats.

The integral form of Eq. (1) for a region Ω with a boundary S can be written as

$$\frac{\partial}{\partial x}\int_\Omega w\,dx\,dy+\oint_S (f\,dy-g\,dx)=0 \tag{6}$$

Received Nov. 19, 1984; presented as Paper 85-0291 at the AIAA 23rd Aerospace Sciences Meeting, Reno, NV, Jan. 14-17, 1985; revision submitted May 17, 1985.

*Research Assistant, Mechanical and Aerospace Engineering.
†Head, Theoretical Aerodynamics Branch, Transonic Aerodynamics Division. Associate Fellow AIAA.
‡Professor, Mechanical and Aerospace Engineering. Associate Fellow AIAA.

The above equation is applied to a cell designated (i, j) of the type indicated in Fig. 1, with the result that the continuity and x-momentum equations can be written as

$$\frac{\partial}{\partial t}(\rho h)_{i,j} + \sum_{k=1}^{4} [\rho_k Q_k]_{i,j} = 0 \tag{7}$$

$$\frac{\partial}{\partial t}(\rho u h)_{i,j} + \sum_{k=1}^{4} [\rho_k u_k Q_k + \Delta y_k p_k]_{i,j} \tag{8}$$

where h is the area of the cell and

$$Q_k = \Delta y_k u_k - \Delta x_k v_k \tag{9}$$

is the flux velocity. The energy equation has a form similar to that of the continuity equation, while the form of the y momentum is similar to that of the x momentum.

Each flux quantity appearing in Eqs. (7) and (8) and similar equations is evaluated as the average of the values in the cells adjacent to the face. Thus, properties along the face separating cells (i,j) and $(i+1,j)$ are given by

$$w_k = \tfrac{1}{2}(w_{i,j} + w_{i+1,j})_k \tag{10}$$

As a result of this, the governing equations can be represented as

$$\frac{dw_{ij}}{dt} + F_{ij}/h_{ij} = 0 \tag{11}$$

For a Cartesian grid with equal cells, the above representation corresponds to central differencing. As is well known, this results in even and odd point oscillations and in overshoots near shock waves. To suppress such a behavior, Jameson et al.[6] introduced second- and fourth-difference dissipation terms. The dissipation terms employed here are the same as those used in Ref. 6 for the interior cells. At the boundaries, the modification developed by Salas et al.[9] is employed.

With the introduction of the dissipation terms, the governing equations can be written as

$$\frac{dw}{dt} + R(w) = 0 \tag{12}$$

where

$$R_{ij} = (1/h_{ij})(F_{ij} - D_{ij}) \tag{13}$$

with D_{ij} being the dissipation term. The Runge-Kutta stepping scheme employed here is that employed in Ref. 8, i.e.,

$$w^{n+1} = w^m \tag{14}$$

with

$$w^m = w^n - \alpha_m \Delta t R_{m-1} \tag{15}$$

For a fourth-order method, $m = 4$ and

$$\alpha_1, \alpha_2, \alpha_3, \alpha_4 = 1/4,\ 1/3,\ 1/2,\ 1 \tag{16}$$

$$R_m = (F_{ij}^m - D_{ij}^0)/h_{ij},\ w^0 = w^n \tag{17}$$

Boundary Conditions

The eigenvalues of A, where

$$A = \partial f/\partial w \tag{18}$$

are u, u, $u+a$, $u-a$, with a being the speed of sound. Thus, at a subsonic inflow boundary, $x = \text{const}$, three eigenvalues are positive and, therefore, three flow properties should be specified and the fourth should be extrapolated from the interior. On the other hand, at a subsonic outflow boundary, three properties are extrapolated from the interior and the fourth is specified. For supersonic flow, all eigenvalues are positive and, thus, four properties have to be specified at inflow, while at outflow all properties have to be extrapolated.

To determine which properties have to be specified and which extrapolated, the scheme employed in Ref. 9, which is based on the method of characteristics for a one-dimensional unsteady flow, was employed. Thus, for a subsonic boundary, $x = \text{const}$, the Riemann variables, G_∞, G_e along the incoming and outgoing characteristics can be written as

$$G_\infty = u_\infty - [2a_\infty/(\gamma-1)] = u_b - [2a_b/(\gamma-1)] \tag{19}$$

$$G_e = u_e + [2a_e/(\gamma-1)] = u_b + [2a_b/(\gamma-1)] \tag{20}$$

where b designates the boundary, ∞ the freestream, and e an extrapolated condition. It follows from Eqs. (19) and (20) that

$$u_b = (G_e + G_\infty)/2,\ a_b = (\gamma-1)(G_e - G_\infty)/4 \tag{21}$$

At an inflow boundary, the tangential, or y, velocity component and a thermodynamic quantity, such as the entropy, are prescribed from the freestream values, while at an outflow boundary these quantities are extrapolated from the interior.

The no-flow boundary condition at a solid surface can be written as

$$v \cdot n = 0 \tag{22}$$

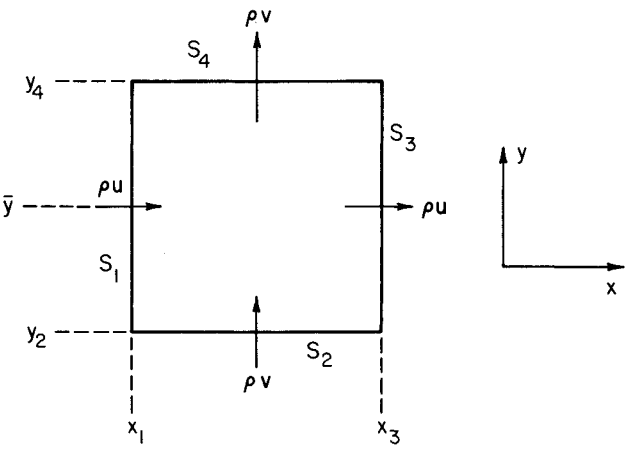

Fig. 1 Interior flux cell.

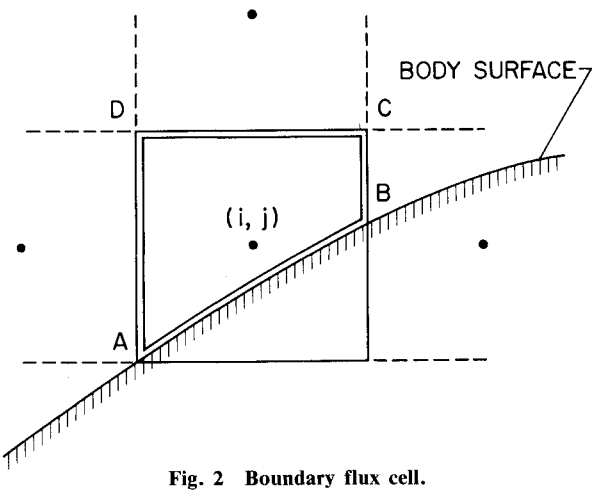

Fig. 2 Boundary flux cell.

where v is the resultant velocity and n is the unit normal. If one considers a boundary cell such as the one indicated in Fig. 2, then Eq. (22) can be implemented exactly if one sets for the side that coincides with the boundary

$$Q_k = 0 \text{ and } p = p_b \tag{23}$$

As a result of Eq. (23), one must express p_b in terms of the other flow variables before commencing with the numerical solution. In this work we experimented with extrapolation of p_b from interior points and with its evaluation from the normal momentum equation

$$\frac{\partial p}{\partial n} = -\rho q^2/\kappa \text{ at the wall} \tag{24}$$

where q is the tangential velocity and κ is the radius of curvature.

The manner in which p_b was calculated will be discussed with reference to the sketch indicated in Fig. 3. As an illustration, let us consider point 3. When the pressure is determined by extrapolation in the y direction, one extrapolates the values of the pressure at 1 and 2 to the y level of point 3. Calculations based on Eq. (24) are more involved. Equation 24 can be written as

$$-\sin\theta\frac{\partial p}{\partial x} + \cos\theta\frac{\partial p}{\partial y} = -\rho q^2/\kappa \tag{25}$$

where $\tan\theta$ is the local body slope. Equation (25) is then solved for $\partial p/\partial x$ or $\partial p/\partial y$, depending on whether $|\tan\theta| \gtrless 1$. Thus, if $|\tan\theta| < 1$, Eq. (25) is written as

$$\frac{\partial p}{\partial y} = \frac{1}{\cos\theta}\left(\sin\theta\frac{\partial p}{\partial x} - \rho q^2/\kappa\right) \tag{26}$$

A one-sided difference is employed to express $\partial p/\partial y$ and $\partial p/\partial x$. Thus, for point 3, points 2 and 3 provide the desired representation for $\partial p/\partial y$. The flow properties ρ and q are determined by extrapolation using points 1 and 2, while points 2 and 4 provide a representation for $\partial p/\partial x$; θ and κ are determined from the airfoil geometry.

Geometry

The area of a cell is given by (see Fig. 1):

$$h = \tfrac{1}{4}(S_x S_y + S_x D_y + S_y D_x - D_x D_y) \tag{27}$$

where

$$S_x = S_1 + S_3, \qquad S_y = S_2 + S_4$$

$$D_x = |S_3 - S_1|, \quad D_y = |S_4 - S_2| \tag{28}$$

The above equation is valid for all rectangular cells and cells intersected by the body, provided the lengths of cell sides contained completely within the body are set equal to zero.

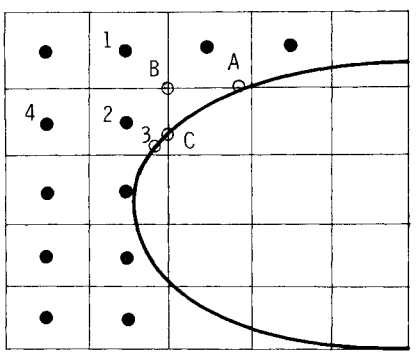

Fig. 3 Sketch of grid in the neighborhood of airfoil.

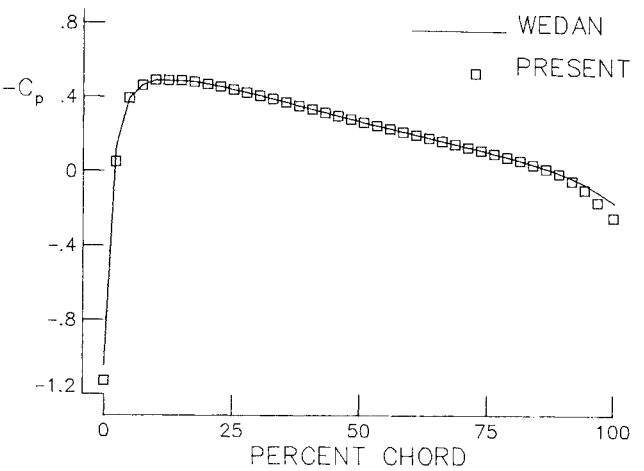

Fig. 4 Comparison of calculated pressure distribution with potential solution ($M = 0.5$, $\alpha = 0$).

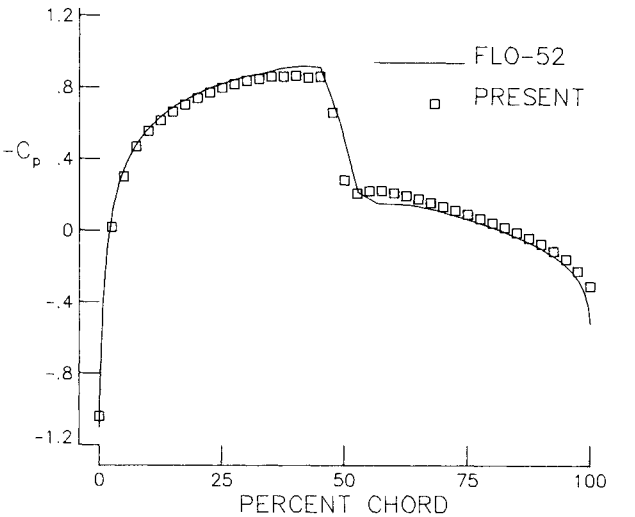

Fig. 5 Comparison of calculated pressure distribution with FL052 ($M = 0.8$, $\alpha = 0$).

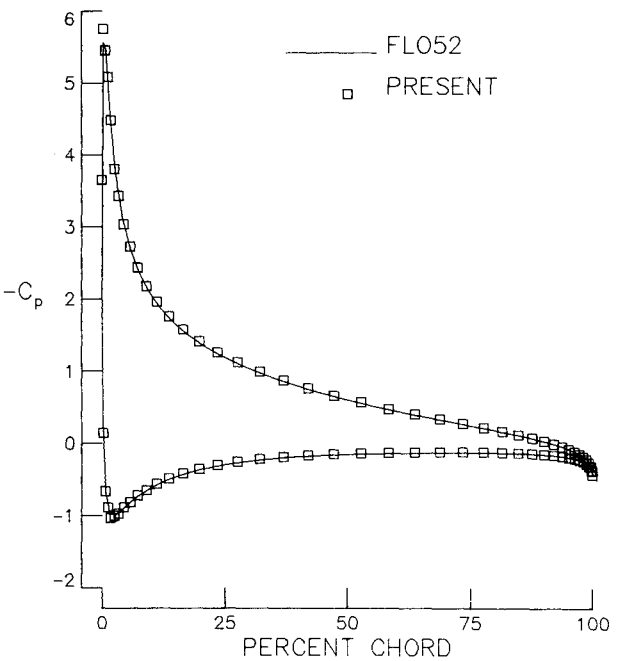

Fig. 6 Comparison of calculated pressure distribution with FL052 ($M = 0.3$, $\alpha = 10$ deg).

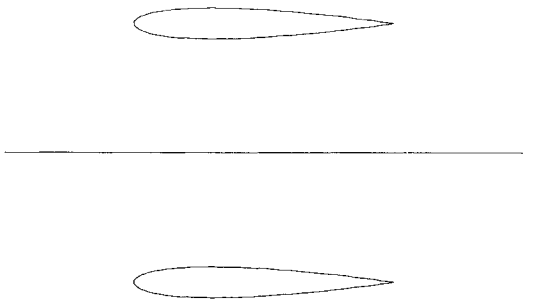

Fig. 7 Schematic of a biplane configuration.

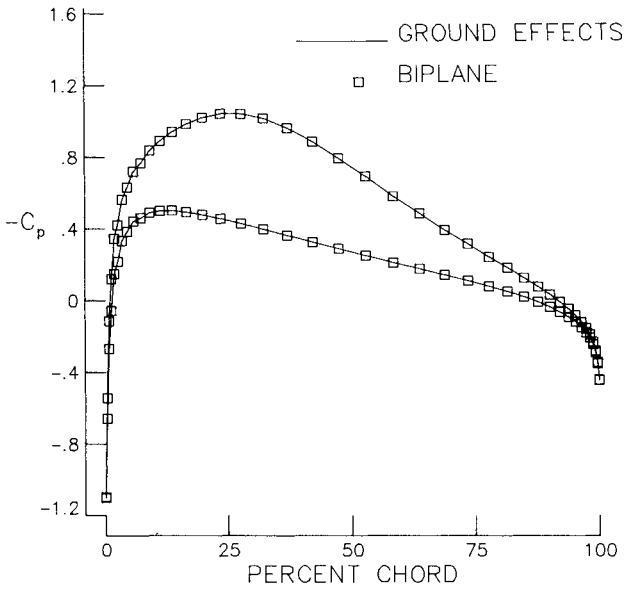

Fig. 8 Comparison of C_p for ground effect and biplane configuration ($M=0.5$, $\alpha=0$).

As is discussed below, it is necessary to cluster grid points in certain critical regions of the flowfield. A spline routine is used to provide a representation of the airfoil and to locate the points of intersection of the grid and the airfoil surface. Because of the manner in which the area of cells is determined, the lengths of cell sides adjacent to the body are modified to include only the portions exterior to the body.

For a body of arbitrary shape, the body-grid intersections may yield cells of small areas adjacent to cells of large areas. If one advances the solution in time based on a local time step, then such an arbitrary distribution of cell areas may result in instabilities. To avoid this problem, small cells such as cell ABC in Fig. 3 (less than 25-50% of a neighboring cell) are incorporated into adjacent cells away from the body.

Results and Discussion

In all the results presented here, p_b was calculated by second-order extrapolation in the y direction. The first case tested consisted of an NACA 0012 airfoil, at various Mach numbers and zero angle of attack, using a coarse grid (68×39) with equal cells around the airfoil. Beyond the airfoil, the coordinates were stretched according to a formula of the type

$$x_{i+1}=x_i+(x_i-x_{i-1})\times1.25$$

The outer boundaries were placed about 10 chord lengths away from the airfoil. Comparisons were made with the results of Ref. 5 and FL052S, which is the version of FL052

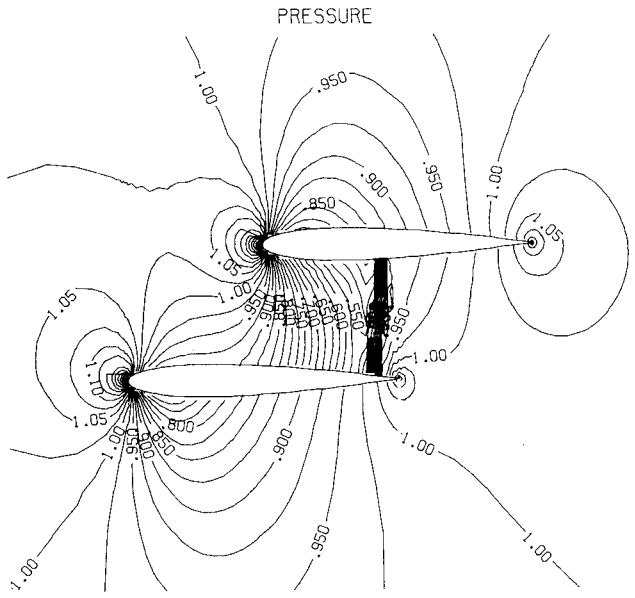

Fig. 9 Pressure contours for a staggered biplane configuration ($M=0.7$, $\alpha=0$).

described in Ref. 9. Because FL052 uses body-fitted coordinates, it was not possible to match grids exactly for the cases compared. Thus, all comparisons with FL052S employed grids that yielded the same number of points on the body.

Figure 4 compares the predictions of this method with those of Ref. 5 for $M=0.5$ and $\alpha=0$, where M is the freestream Mach number and α is the angle of attack. Figure 5 compares our results with FL052S for $\alpha=0$ and $M=0.8$. The drag count for FL052S is 84, while the corresponding number for the present method is 156. This is due to the lack of resolution at the leading and trailing edges. The present solution resolves the shock better because the grid is finer than that of FL052S there.

Coarse grids and equal cell sizes around the body were found to be inappropriate when one tries to calculate flowfields at high angles of attack. Fine grids and grid clustering is required for such cases; otherwise, it is not possible to satisfy the Kutta condition. Figure 6 compares the prediction with that of Ref. 9 for the case of $\alpha=10$ and $M=.3$. Again, good agreement is observed. The grid employed in this case is 78×47. The drag count for FL052S is 218, while the present method gives 241. This demonstrates that the discrepancy in the drag count indicated above for Fig. 5 is solely a result of lack of clustering around the leading and trailing edges.

Now that the first two objectives of this work have been demonstrated, we proceed to show the manner in which the third objective, namely, calculating flowfields past multielement airfoils, has been achieved. In an effort to verify the feasibility of the approach, calculations are presented for $M=0.5$ and $\alpha=0$ for the biplane configuration indicated in Fig. 7. As a first step, calculations were carried out for the upper half of the configuration, i.e., for a single airfoil placed about half a chord from the "ground," or wall of symmetry. Later, calculations were carried out for the complete configuration. Figure 8 compares the pressure distribution for the two geometries. It is seen that identical results are obtained.

The next case considered is that indicated in Fig. 9, which shows a staggered biplane configuration, together with pressure contours for $M=0.7$ and $\alpha=0$. The pressure distributions for the individual airfoils are shown in Fig. 10.

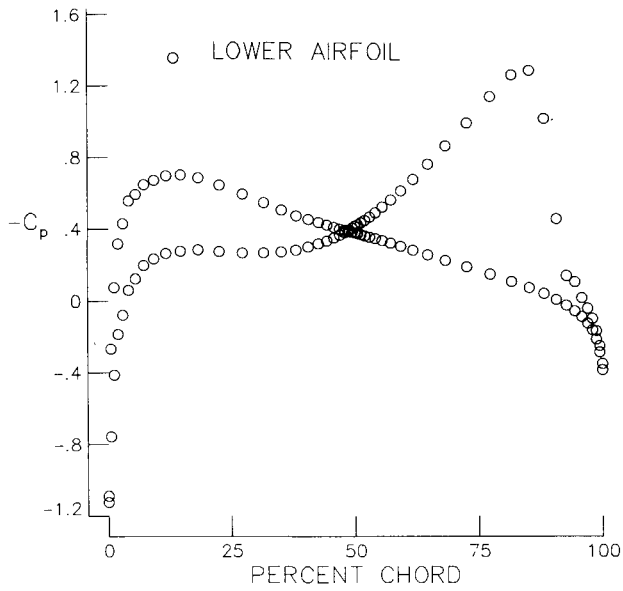

Fig. 10a Pressure distribution on forward airfoil of Fig. 9.

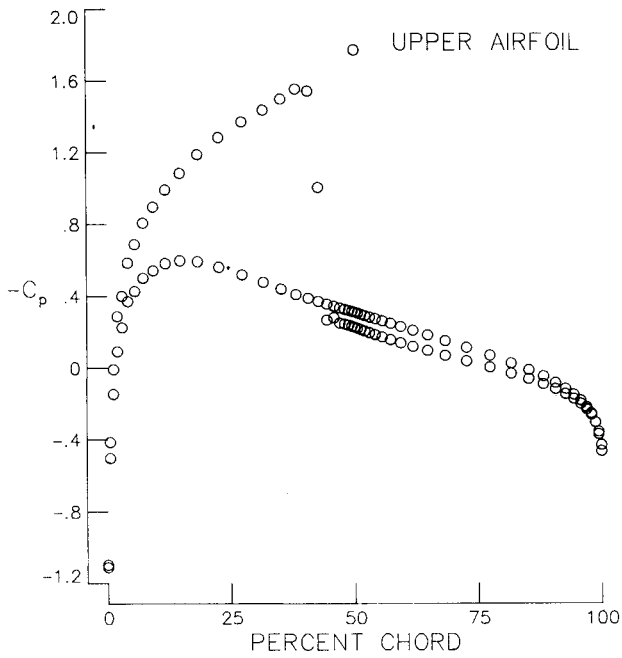

Fig. 10b Pressure distribution on aft airfoil of Fig. 9.

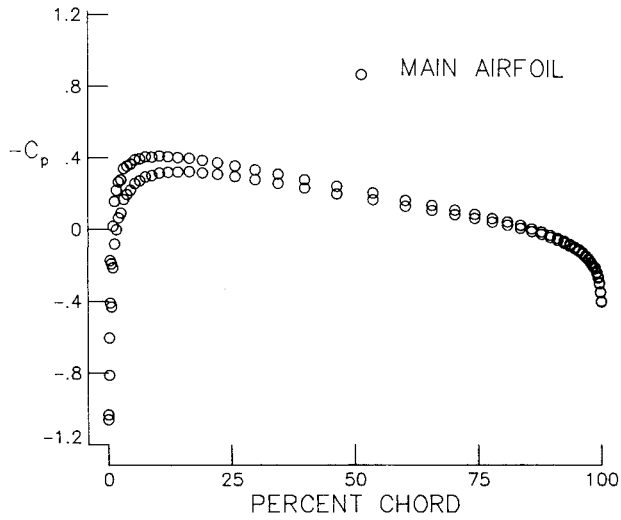

Fig. 12a Pressure on main airfoil of Fig. 11.

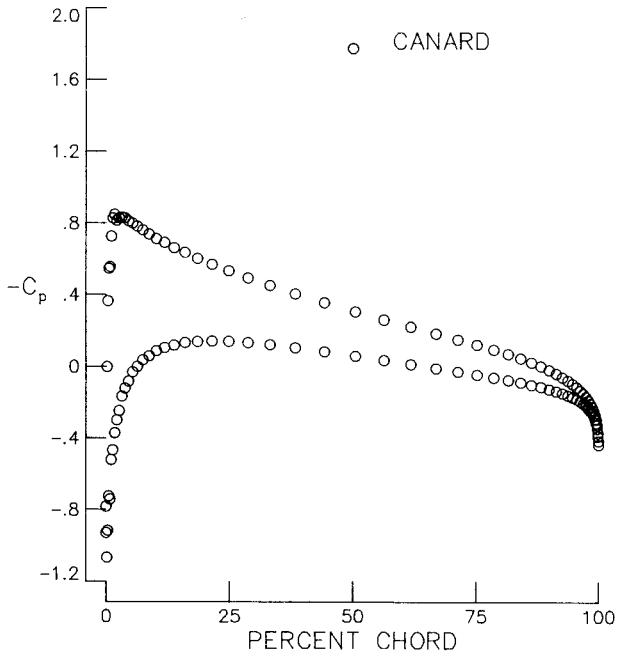

Fig. 12b Pressure on canard.

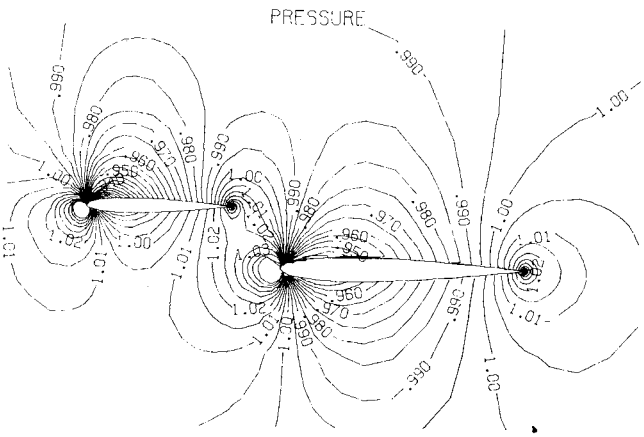

Fig. 11 Pressure contours for canard configuration ($M = 0.5$, $\alpha = 1$ deg).

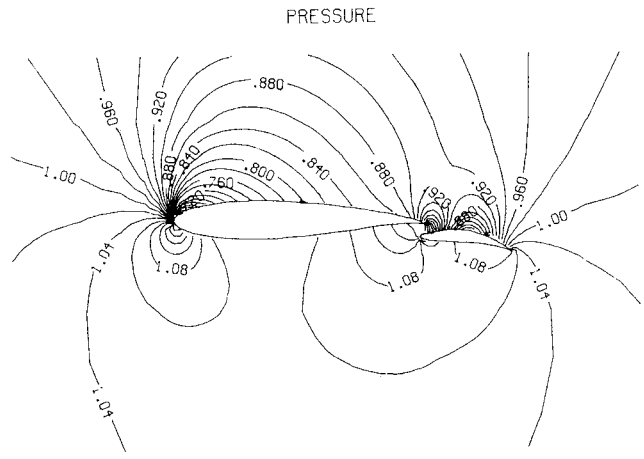

Fig. 13 Schematic of a von Kármán-Trefftz airfoil with flap.

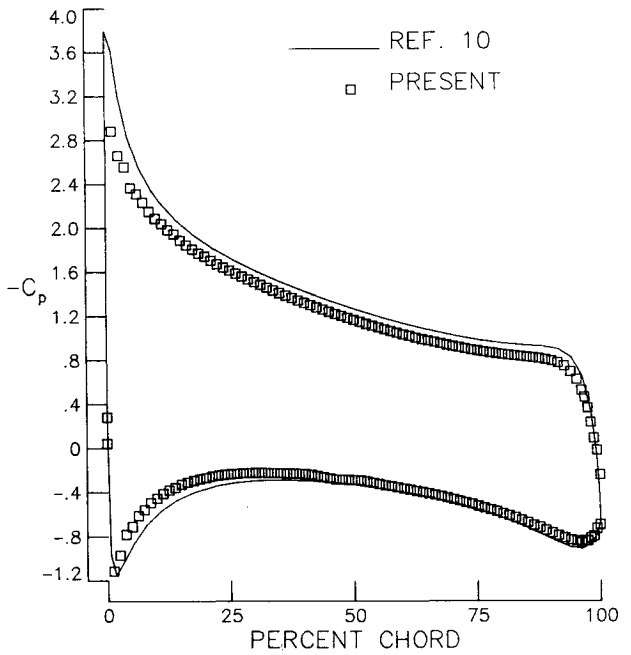

Fig. 14a Comparison of calculated pressure distribution on flap with (compressibility-corrected) exact incompressible solution ($M=0.5$).

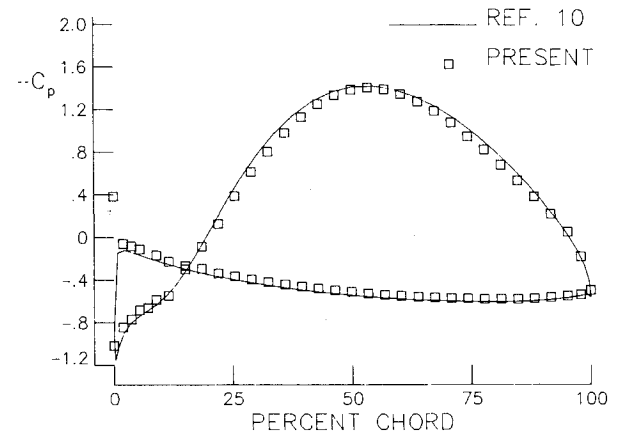

Fig. 14b Comparison of calculated pressure distribution on airfoil with (compressibility-corrected) exact incompressible solution ($M=0.5$).

Although the flow is subcritical for a single NACA 0012 at $M=0.7$ and $\alpha=0$, a shock forms between the two airfoils. The strength of the shock is dependent on the relative positions of the two airfoils. It is interesting to note that, in spite of the shock formation between the inner surfaces, the pressure distributions on the outer surfaces are similar to those of the single airfoil.

The next case considered is that of the canard configuration indicated in Fig. 11. Both the canard and main airfoil are NACA 0010 sections. The pressure distribution for $M=0.5$ and $\alpha=1$ deg is shown in Fig. 12. Again, the results appear to be reasonable.

The final case considered is that of a von Kármán-Trefftz airfoil with a flap, as shown in Fig. 13. The pressure distribution indicated in Fig. 14 is for a zero angle of attack, a flap deflection of 10 deg, and $M=0.5$. An exact calculation for this configuration for incompressible flows was performed by Williams.[10] The results in Fig. 14 are compared with those of Ref. 10 after incorporating the Prandtl-Glauert correction to allow for the effects of compressibility. Good agreement is indicated. The discrepancy indicated around the leading edge of the main airfoil is a result of the coarse grid there.

Concluding Remarks

The work presented here confirms the findings of Wedan and South regarding the simplicity and utility of using Cartesian grids in conjunction with a finite volume formulation for the solution of a variety of fluid flow problems. The many applications presented here demonstrate the accuracy and robustness of the method. Although a Runge-Kutta time-stepping algorithm was employed, the method can be used with other algorithms.

Acknowledgments

This work was supported in part by NASA Cooperative Agreement NCCI-22. The authors would like to acknowledge many helpful discussions with Bruce Wedan, Vigyan Research Associates, Inc. and Jerry C. South Jr., Chief Scientist, NASA Langley Research Center.

References

[1]Thompson, Joe F., Warsi, Z.U.A., and Mastin, C.W., "Boundary Fitted Coordinate Systems for Numerical Solution of Partial Differential Equations—A Review," *Journal of Computational Physics*, Vol. 47, July 1982, pp. 1-108.

[2]Jameson, A. and Caughey, D.A., "Finite Volume Method for Transonic Potential Flow Calculations," AIAA Paper 77-635, 1977.

[3]Jameson, A. and Caughey, D.A., "Progress in Finite Volume Calculations for Wing-Fuselage Combinations," *AIAA Journal*, Vol. 18, Nov. 1980, pp. 1281-1288.

[4]Purvis, J.W. and Burkhalter, J.E., "Prediction of Critical Mach Number for Store Configurations," *AIAA Journal*, Vol. 17, Nov. 1979, pp. 1170-1177.

[5]Wedan, B. and South, J.C. Jr., "A Method for Solving the Transonic Full-Potential Equation for General Configurations," AIAA Paper 83-1889, 1983.

[6]Jameson, A., Schmidt, W., and Turkel, E., "Numerical Solutions of the Euler Equations by Finite Volume Methods Using Runge-Kutta Time-Stepping Schemes," AIAA Paper 81-1259, 1981.

[7]Jameson, A. and Baker, T.J., "Solution of the Euler Equations for Complex Configurations," AIAA Paper 83-1829, 1983.

[8]Jameson, A. and Baker, T.J., "Multigrid Solution of the Euler Equations for Aircraft Configurations," AIAA Paper 84-0093, 1984.

[9]Salas, M.D., Jameson, A., and Melnik, R.E., "A Comparative Study of the Nonuniqueness Problem of the Potential Equation," AIAA Paper 83-1888, 1983.

[10]Williams, B.R., "An Exact Test Case for the Plane Potential Flow About Two Adjacent Lifting Aerofoils," Aeronautical Research Council, R&M 3717, 1973.